Archives of Acoustics Vol. 48, No. 3, pp. 389–401 (2023), doi: 10.24425/aoa.2023.145245

Research Paper

An Improved EMD Method Based on Utilizing Certain Inflection Points in the Construction of Envelope Curves

Mohsen KAFIL[(1),(2)*], Kaveh DARABI[(2)], Saeed ZIAEI-RAD[(3)]

[(1)] *Mechanical Engineering Group, Pardis College, Isfahan University of Technology*
Isfahan, Iran

[(2)] *Mobarakeh Steel Company*
Isfahan, Iran

[(3)] *Department of Mechanical Engineering, Isfahan University of Technology*
Isfahan, Iran

*Corresponding Author e-mail: mohsen.kafil@gmail.com

(*received July 17, 2022; accepted February 11, 2023*)

The empirical mode decomposition (EMD) algorithm is widely used as an adaptive time-frequency analysis method to decompose nonlinear and non-stationary signals into sets of intrinsic mode functions (IMFs). In the traditional EMD, the lower and upper envelopes should interpolate the minimum and maximum points of the signal, respectively. In this paper, an improved EMD method is proposed based on the new interpolation points, which are special inflection points (SIP_n) of the signal. These points are identified in the signal and its first $(n-1)$ derivatives and are considered as auxiliary interpolation points in addition to the extrema. Therefore, the upper and lower envelopes should not only pass through the extrema but also these SIP_n sets of points. By adding each set of SIP_i $(i = 1, 2, ..., n)$ to the interpolation points, the frequency resolution of EMD is improved to a certain extent. The effectiveness of the proposed SIP_n-EMD is validated by the decomposition of synthetic and experimental bearing vibration signals.

Keywords: empirical mode decomposition (EMD); interpolation points; envelope curve; inflection points; rolling element bearing fault diagnosis.

1. Introduction

One of the most powerful methods in dealing with nonlinear and non-stationary time series is the Hilbert–Huang transform (HHT), introduced by Huang *et al.* (1998). The HHT procedure consists of two parts. At the first step, the empirical mode decomposition (EMD) process adaptively decomposes a complicated multi-component signal into sets of mono-component intrinsic mode functions (IMFs), which can admit well-behaved Hilbert transform. In the second step, the Hilbert spectral analysis (HSA) is performed on each IMF and the instantaneous amplitude and frequency of all IMFs are computed.

The major deficiency of the traditional EMD is the mode mixing phenomenon, which is defined as the appearance of signals at very different scales in one IMF or the distribution of a specific scale signal among different IMFs. Some researchers have proposed creative approaches to solve this problem, including ensemble empirical mode decomposition (EEMD) (Wu, Huang, 2009), complete ensemble empirical mode decomposition (CEEMD) (Yeh *et al.*, 2010), complete ensemble empirical mode decomposition with adaptive noise (CEEMDAN) (Torres *et al.*, 2011), ensemble noise-reconstructed EMD method (ENEMD) (Yuan *et al.*, 2013), high-fidelity noise-reconstructed empirical mode decomposition (HNEMD) (Yuan *et al.*, 2022), EMD manifold (Wang *et al.*, 2020), and other.

EMD is an iterative process with interpolation as its central part. At each step of the iteration, all local maxima and minima of the signal are obtained and

then interpolated to construct the envelope curves. Although the above-mentioned methods have shown great improvement in the mode mixing problem, utilizing maxima and minima as the interpolation points remains an unchanged rule among them. Little research has been so far carried out on utilizing other interpolation points to construct envelope curves in the EMD process, so further studies are still needed in this area. Since there is no difference between the traditional EMD, EEMD, and CEEMD methods in terms of the selection of extrema as the interpolation points, this paper only focuses on the traditional EMD method. Furthermore, the traditional EMD has another advantage, i.e., the main signal is not repeatedly affected by different random noises.

By using the genetic algorithm, Kopsinis and McLaughlin (2007; 2008) showed that the performance of EMD will be improved if envelope curves pass through the extrema of the highest instantaneous frequency component of the signal instead of the extrema of the signal itself. Xu *et al.* (2010) presented a piecewise-defined quadratic interpolation in which the position information of minimum points (maximum points) is used in the construction of the upper envelope (lower envelope). Hence the upper envelope (lower envelope) not only passes through the maxima (minima) but also through the intersection points of the lines connecting the maxima (minima) with the vertical lines going through the minima (maxima). The extrema detection method is an important matter, especially in the presence of noise, so Bouchikhi and Boudraa (2012) introduced a new version of EMD, which is more robust to noise since the envelopes of the signal are constructed using smoothing B-splines instead of exact interpolation methods. Chu *et al.* (2012) proposed an envelope curve that interpolates the main and pseudo extrema by the quartic Hermitian polynomial interpolation method. Singh *et al.* (2014) introduced an EMD algorithm based on pseudo extrema and nonpolynomial spline interpolation. Instead of calculating the mean of the upper and lower envelopes, Wang and Li (2013) proposed to calculate the mean values directly by interpolating the midpoints of line segments, connecting each maximum (minimum) to its two neighboring minima (maxima). Li *et al.* (2015a) used a similar method but replaced the cubic spline interpolation with the cubic B-spline. Zhao *et al.* (2017) put forward adjustable cubic trigonometric cardinal spline interpolation for the direct construction of the mean curve. Efforts have also been made to define a suitable envelope for the EMD method. For instance, Yang *et al.* (2014) presented a new model of the envelope by using convex constraint optimization.

In this paper, we introduce a special set of inflection points as the auxiliary interpolation points for the construction of the envelope curves. These special inflection points (SIPs), as well as how to distinguish them from other inflection points, will be discussed later in Sec. 3. The popular cubic spline is applied as the interpolation function in this paper. The cubic spline is a continuous function and has continuous first and second derivatives. Two boundary conditions should also be met at the left and right sides of the signal. We utilize here the not-a-knot boundary condition, which requires the continuity of the third derivative at the second and second to last points.

The rest of this paper is organized as follows: the main procedure and adjustable parameters of the traditional EMD algorithm are explained in Sec. 2. Sections 3 and 4 describe the theoretical aspects of our new method. In Sec. 3, the SIP_n points of a signal are defined and the differences between the traditional and new envelopes are shown. The additional required steps for the proposed EMD method are described in Sec. 4. In Sec. 5, the performance of the proposed EMD method is verified for numerous two-tone signals and a real vibration signal of a rolling element bearing and the decomposition results are compared with the traditional EMD. Finally, a brief conclusion is provided in Sec. 6.

2. Empirical mode decomposition (EMD) algorithm

The EMD algorithm decomposes a signal into several IMFs and a final residual, which is the trend of the signal. The extraction process for each IMF is called the sifting process. The IMFs are expected to simultaneously meet the following two conditions (Huang *et al.* 1998): 1) in the whole data set, the number of extrema and the number of zero crossings should be equal or differ at most by one; 2) the mean value of the envelope defined by the local maxima (upper envelope) and the envelope defined by the local minima (lower envelope) should be approximately zero, at any point. In practice, the definition of the term "zero" in the second condition should be defined more clearly and it is better to evaluate the amplitude of the mean compared to the amplitude of the extracted mode. The traditional EMD steps are as follows:

1) Initialize $r_0 = y$, where y is the main signal.
2) Initialize $i = 1$ and $k = 1$, where i counts the number of IMFs, and k counts the number of sifting iterations for each IMF.
3) Set $h_{i(k-1)} = r_{(i-1)}$.
4) Identify all local maxima of $h_{i(k-1)}$ and interpolate them by cubic spline to construct the upper envelope. Similarly, construct the lower envelope by interpolating minima.
5) Calculate the mean $m_{i(k-1)}$ of the upper and lower envelopes and subtract it from $h_{i(k-1)}$ to obtain $h_{ik} = h_{i(k-1)} - m_{i(k-1)}$.

6) If h_{ik} satisfies the stop-sifting criteria, set $\mathrm{IMF}_i = h_{ik}$; else set $k = k + 1$ and go to step (4).
7) Set $r_i = r_{(i-1)} - \mathrm{IMF}_i$.
8) If the number of extrema of r_i is less than three or the desired number of IMFs is extracted, the decomposition process is finished. Otherwise, first set $i = i + 1$, $k = 1$, and then go to step (3).

Therefore, the given signal $y(t)$ is decomposed into several IMFs and a final residual r_N as follows:

$$y(t) = \sum_{i=1}^{N} \mathrm{IMF}_i(t) + r_N(t). \tag{1}$$

The EMD method is an adjustable algorithm and can be improved by several approaches, such as optimizing the method of interpolation, adjusting the stopping criteria for the sifting process, changing the end conditions of the signal, and selecting new sets of interpolation points instead of signal's extrema.

Various interpolation methods have been proposed so far. The well-known cubic spline is the first and most widely used one (Huang *et al.*, 1998), but other methods such as B-splines (Bouchikhi, Boudraa, 2012; Chen *et al.*, 2006; Wang, Li, 2013), cubic and quartic Hermite (Chu *et al.*, 2012; Li *et al.*, 2015b; Guo, Deng, 2017), Akima interpolation (Egambaram *et al.*, 2016), power function (Qin, Zhong, 2006), rational splines (Pegram *et al.*, 2008), cubic trigonometric cardinal spline (Zhao *et al.*, 2017), cubic trigonometric B-spline (Li *et al.*, 2018) and nonpolynomial spline (Singh *et al.*, 2014) have also been employed.

To generate physically meaningful IMFs, an accurate stopping criterion should be defined. At least four stopping criteria for the sifting process have been introduced so far (Huang *et al.*, 1998; 2003; Wu, Huang, 2009; Rilling *et al.*, 2003). In this paper, the criterion introduced by Rilling *et al.* (2003) is used. They substituted the second condition of the IMF for a more practical one by defining the relative mean as follows:

$$\sigma(t) = \left| \frac{\mathrm{env}_{\max}(t) + \mathrm{env}_{\min}(t)}{\mathrm{env}_{\max}(t) - \mathrm{env}_{\min}(t)} \right|, \tag{2}$$

where $\mathrm{env}_{\max}$ and $\mathrm{env}_{\min}$ are the upper and lower envelopes, respectively and $\sigma(t)$ is the ratio of the mean of the upper and lower envelopes to the half distance of them. The sifting is iterated until (1) $\sigma(t) < \theta_1$ for a predetermined fraction α of the signal and (2) $\sigma(t) < \theta_2$ for the total length of the signal. Common values for the thresholds and fraction are $\theta_1 = 0.01$, $\theta_2 = 0.1$, and $\alpha = 0.99$. The first condition guarantees a globally small fluctuation of the mean because the relative mean becomes smaller than 0.01 for at least 99% of the signal. The second condition prevents locally large deviation of the mean because there is no part of the signal in which the relative mean exceeds the value 0.1.

The endpoints of the signal are not necessarily its extrema. Since the envelope curves should pass through the extrema, some boundary extrema should be extended beyond the existing data range. In this paper, we use the reflection method proposed by Rilling *et al.* (2003). Without mirroring, considerable distortions at two ends of IMFs may emerge. This phenomenon is called the end effect of the EMD method (Lei *et al.*, 2013).

3. Special inflection points (SIP)

The EMD algorithm considers a signal as the superposition of some fast and some slow oscillating parts. After extracting the fastest oscillating part, the algorithm considers the remainder as a new signal. This process continues until just the slowest oscillating part remains. Oscillation, in signal processing terminology, refers to a repeated variation of a measured quantity. Repetition immediately brings into mind the concept of extrema. On this basis, the EMD algorithm first detects the extrema and then passes the upper and lower envelopes just through the detected extrema. By subtracting the mean of the lower and upper envelopes, the EMD indeed separates the slower detectable oscillating parts from the signal, step by step. The appearance of extrema plays a very important role in the EMD method. Some researchers believe that EMD can only extract a component if it can detect extrema that are related to it (Rilling, Flandrin, 2007). However, the origins of some oscillations are difficult to trace with the extrema alone. In these cases, the inflection points can be used as auxiliary points along with extrema to detect the oscillations. To investigate this claim, consider a simple composite signal, which consists of linear and harmonic components as follows:

$$y(t) = \alpha t + \cos(2\pi t), \tag{3}$$

where α is an arbitrary constant. The time of occurrence of the extrema can be calculated by:

$$t_E = \frac{1}{2\pi} \sin^{-1}\left(\frac{\alpha}{2\pi}\right) + n, \qquad n = 0, 1, 2, \ldots. \tag{4}$$

If $\alpha \le 2\pi$, the signal can be easily decomposed into its two components, but if $\alpha > 2\pi$, EMD cannot decompose the signal because y is a monotonically increasing function and it does not have any extrema. Although there is no fundamental difference between the two cases with $\alpha = (2\pi)^+$ and $\alpha = (2\pi)^-$, the traditional EMD algorithm treats them entirely differently. This is because of the insistence on using the first derivative of the signal (extremum points) in the traditional EMD and neglecting higher-order derivatives (for example, inflection points). Figure 1 shows this signal for eight different values of α. The minimum, maximum, and inflection points in the time range from 1 to 1.5 s are

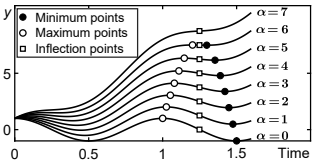

Fig. 1. Convergence of the maximum and minimum points in the signal $y(t) = \alpha t + \cos(2\pi t)$ with increasing α.

demonstrated by the black circles, white circles, and white rectangles, respectively. As α increases, the maximum and minimum points converge on each other and meet at the inflection point. In the uppermost curve, where α equals 7, there are no extrema, but from the oscillation point of view, the signal behaves similarly to the other cases. A closer look at Fig. 1 reveals that the inflection point of the uppermost curve differs from those of the other curves because it is not surrounded by two extrema. This leads us to the concept that in the local absence of extrema, the oscillatory motion can still be realized by the inflection points. However, only finite sets of inflection points should be determined as auxiliary points along with extrema to construct the envelope curves. By considering the arrangement pattern of extrema and inflection points, these special inflection points are identified. The first SIP_1 of a signal can be defined as follows.

An inflection point of a signal is its SIP_1 if, by moving away from that point toward either the left or right directions, we first reach another inflection point before reaching an extremum. We can generalize this definition to SIP_n in the same fashion. The SIP_n of a signal is the SIP_1 of the $(n-1)$-th derivative of the original signal.

For example, in a simple sine function, after each maximum, the signal starts to decrease and is forced to change its curvature sign before reaching the minimum point. Hence, in the sine function, every inflection point is always located between two extrema and thus there is not any SIP_n in the simple sine function. There should be more than two inflection points between two successive extrema to generate SIP_1. To demonstrate SIP_n graphically, consider a two-component signal in the form of

$$y(t) = \cos(2\pi t) + a_r \cos(2\pi f_r t), \tag{5}$$

where a_r is the amplitude ratio and f_r is the frequency ratio of the two components. We have plotted these signals and their first and second derivatives for $a_r = 2$ and $a_r = 4$ in the left and right columns of Fig. 2, respectively. The frequency ratio is considered as $f_r = 0.65$ for both of them. These signals are two simple numerical examples to clarify the graphical interpretation of SIP_1 and SIP_2. By determining the location of extrema and inflection points of the first signal, i.e., $a_r = 2$, one SIP_1 is detected at $t \cong 1.357$ and

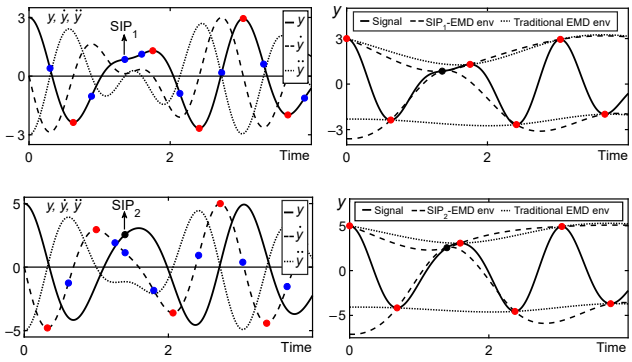

Fig. 2. Appearance of SIP_1 and SIP_2 points in two simple signals. In all curves, red, blue, and black circles represent extrema, inflection points, and SIP_n, respectively. Top row: the two-component signal with $f_r = 0.65$ and $a_r = 2$ in the left and with $f_r = 0.65$ and $a_r = 4$ in the right column with their first and second derivatives. Bottom row: the traditional EMD envelopes (dotted line), SIP_1-EMD envelopes in the left (dashed line), and SIP_2-EMD envelopes in the right column (dashed line).

shown in the left top diagram. It is a SIP_1 because it is surrounded by two other inflection points (blue circles) and not two extrema (red circles). For the second signal, i.e., $a_r = 4$, the extrema and inflection points of its first derivative are determined, which leads to detecting one SIP_2 at $t \cong 1.4$, shown in the right top diagram. It is a SIP_2 of the main signal because it is a SIP_1 of the first derivative of the signal. It should be noted that the frequency and amplitude ratios of these signals are selected in such a way that the first signal has just one SIP_1 and the second has just one SIP_2, but in general, there may be any number of SIP_n points in an arbitrary signal.

The bottom row of Fig. 2 compares the envelopes of the traditional EMD with those of the SIP_n-EMD. In the SIP_n-EMD method, both the upper and lower envelopes should pass through all the SIP_n points. It may seem a little unreasonable that both envelopes pass through a common point. However, Fig. 1 shows how two successive minimum and maximum points converge to one SIP_1, so we can suppose one SIP_1 as two infinitely close maximum and minimum points that coincide with each other.

The performance of the SIP_1-EMD and the traditional EMD in separating the first component of the previous two-component signal with $a_r = 2$ and $f_r = 0.65$ has been shown in the left and right column diagrams of Fig. 3, respectively. To provide a better comparison, the main signal $(\cos(2\pi t) + 2\cos(2\pi \times 0.65t))$ and the higher frequency component $(\cos(2\pi t))$ have been plotted in all diagrams with black continuous and red dotted lines. The output of the decomposition (h_{1k}) after the first, tenth, and hundredth sifting iterations $(k = 1, 10, 100)$ has been drawn with the blue lines in the first, second, and third rows, respec-

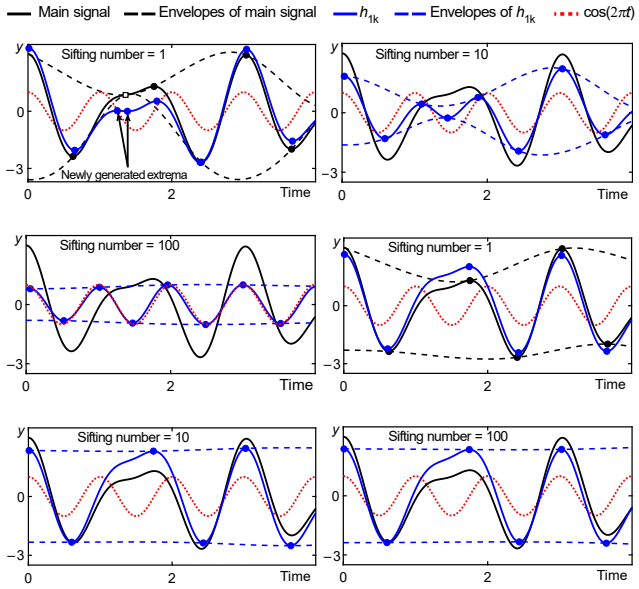

Fig. 3. Performance comparison of the SIP_1-EMD (left column) and the traditional EMD (right column) methods for the case $y = \cos(2\pi t) + 2\cos(2\pi \times 0.65t)$. In all diagrams, the continuous and dashed black lines represent the main signal and its envelopes, the continuous and dashed blue lines represent h_{1k} and its envelopes and dotted red lines represent the first component ($\cos(2\pi t)$). Black and blue circles demonstrate extrema in all curves, and the SIP_1 point is shown by one white rectangle. The top, middle, and bottom rows are related to the first, tenth, and hundredth sifting iterations (k = 1, 10, and 100), respectively.

tively. The main signal has one SIP_1 at $t \cong 1.357$, which is demonstrated with a white rectangle in the left column, top row diagram. Both upper and lower envelopes pass through it and immediately after one sifting iteration, one maximum and one minimum point are generated in h_{11} before and after the SIP_1 at $t \cong 1.242$ and $t \cong 1.383$. These two newly generated extrema help the h_{1k} get closer and closer to the first component. In the third row of the left column, after 100 iterations, the h_{1-100} almost coincides with the first component, which is the desired result. As can be seen in the right column, the traditional EMD is completely unable to decompose this signal. As the number of sifting iterations increases, instead of approaching the first component, h_{1k} moves away from it. Since the upper and lower envelopes of h_{1-100} in the right column are two parallel horizontal lines, there would be no point in continuing the sifting process.

4. SIP_n-EMD method

The main difference between our proposed EMD method in this paper and the traditional EMD is in step (4) of the previously mentioned steps. We develop the SIP_n-EMD method by extending step (4) of the traditional EMD as:

a) Identify all local maxima and local minima of $h_{i(k-1)}$, similar to the traditional EMD.

b) Take the first derivative of $h_{i(k-1)}$ and find all local minima and local maxima of $\dot{h}_{i(k-1)}$. These points are the inflection points of $h_{i(k-1)}$ and the SIPs of $h_{i(k-1)}$ should be selected from them. This set of points will be referred to as SIP_1.

c) Take the second derivative of $h_{i(k-1)}$ and find all local minima and local maxima of $\ddot{h}_{i(k-1)}$. These points are the inflection points of $\dot{h}_{i(k-1)}$ and the SIPs of $\dot{h}_{i(k-1)}$ should be selected from them. This set of points will be referred to as SIP_2.

d) Repeat this process n times. In the n-th step, take the nth derivative of $h_{i(k-1)}$ and find all local minima and local maxima of $\frac{d^n h_{i(k-1)}}{dt^n}$. These points are the inflection points of the $(n-1)$-th derivative of $h_{i(k-1)}$ and the SIPs should be selected from them. This set of points will be referred to as SIP_n.

e) Pass the upper envelope through the maxima and SIP_1, SIP_2, ..., SIP_n. Similarly, the lower envelope should pass through the minima and SIP_1, SIP_2, ..., SIP_n. Go to step (5) of the traditional EMD.

Theoretically, the SIP_n-EMD method can be extended to n-th derivatives and each new set of SIP_i ($i = 1, 2, ..., n$) should improve the performance of this method. But since differentiation is a noise amplifying process, in practice, after some order of derivatives, the disadvantages of the additive noise outweigh the advantages of new SIP_n points. Hence, in this paper, we have restricted the procedure to extract SIP_1 and SIP_2 for the synthetic signals and SIP_1 for the real-world signals. When extracting the SIP_2 at step (c), we use a simple low pass filter in order to eliminate the additive noise induced by an extra differentiation made in this step.

5. Practical application

In this section, the aim is to compare the ability of the traditional and proposed EMD method to decompose some synthetic and real signals, including a general form of two-tone signals and a vibration signal of a rolling bearing. All calculations have been performed using MATLAB software.

5.1. Two-tone signals

We rewrite the general form of a two-tone signal here again as:

$$y(t) = C_1(t) + C_2(t) = \cos(2\pi t) + a_r \cos(2\pi f_r t), \quad (6)$$

where $t = [0 : 0.001 : 15]$ is the time vector, a_r is the amplitude ratio, f_r is the frequency ratio ($0 < f_r < 1$),

and C_1 and C_2 are two components of the signal. Because the frequency ratio is limited to change in the range from zero to one, C_1 and C_2 are the higher frequency (HF) and lower frequency (LF) components, respectively. The performance of the traditional EMD algorithm on the decomposition of this signal has been previously studied (Rilling *et al.*, 2003; Rilling, Flandrin, 2007).

At first sight, it may be expected that the first and second IMFs should be matched with the HF and LF components, respectively. However, this assumption will not be true for a wide range of frequency and amplitude ratios. In practice, depending on the adjustable parameters of the EMD, one, two, or more IMFs may be extracted. If only one IMF is obtained, it means that the EMD method cannot decompose the signal, and both components are considered as a whole. This is not always a weak point because, in the EMD algorithm, there is a greater emphasis on extracting zero-mean components versus extracting sinusoidal functions. For example, if $a_r = 1$ and $f_r \cong 1$, the superposition of two close tones may be interpreted as a zero-mean amplitude modulation signal, which is not a false interpretation, and in some cases (such as beat phenomenon), may even make more sense (Rilling, Flandrin, 2007; Deering, Kaiser, 2005). If two IMFs are extracted, the decomposition has probably been well conducted, and the first and second IMFs are related to the HF and LF components, respectively. But there is still a possibility of mode mixing. If more than two IMFs are obtained, mode mixing will certainly occur, and at least one, if not all, of the extracted IMFs, will deviate from the signal's components. So, even for this simple signal, several possibilities may arise after the EMD analysis. To eliminate the ambiguity caused by the number of extracted modes, only the first IMF will be extracted here for a two-tone signal. The tone separation error (TSE) will be assessed based only on the first IMF according to the following formula (Rilling, Flandrin, 2007):

$$\mathrm{TSE} = \frac{\|I_1 - C_1\|_2}{\|C_2\|_2}, \tag{7}$$

where I_1 is the first IMF and $\|.\|_2$ stands for the Euclidean norm. In the case of perfect separation of the two components, the first IMF matches the first component thoroughly, so TSE becomes zero. On the other hand, if the EMD method cannot detect the HF component at all and no decomposition is possible, the first IMF matches the main signal thoroughly, so TSE becomes one. It should be noted that, by the definition of TSE, it is not limited to changes between zero and one. However, it would not become much greater than one. This claim is based on experience and there is not any mathematical constraint on the upper value of TSE.

Figure 4 illustrates TSE values on the $(a_r - f_r)$ plane with more than 100 000 different signals. The white and black areas present the minimum (zero) and maximum (a little more than one) errors, respectively. The decomposition process of the top, middle and bottom diagrams, has been simulated by the traditional EMD, SIP_1-EMD, and SIP_2-EMD methods, respectively. For all diagrams, 10 fixed sifting iterations are considered stop-sifting criteria. Moreover, all steps of the EMD method have been carried out in the time range from 0 to 15 s, but the values of TSE have been calculated from 0 to 10 s, so relatively large end effect errors at the right side of the signal vanished in the TSE calculations.

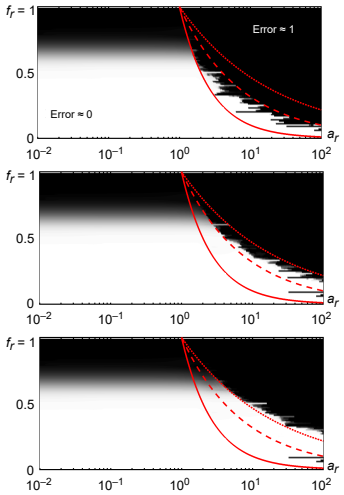

Fig. 4. TSE values on the $(a_r - f_r)$ plane with 10 fixed number of sifting iterations and three border curves, plotted by the continuous $(a_r f_r = 1)$, dashed $(a_r f_r^2 = 1)$, and dotted $(a_r f_r^3 = 1)$ red lines. Top – traditional EMD; middle – SIP_1-EMD; bottom – SIP_2-EMD.

The top diagram, which corresponds to the traditional EMD algorithm, has been previously presented by Rilling and Flandrin (2007). We show it here to compare it with diagrams of our proposed EMD method. As can be seen, the EMD always performs well at the beginning of the frequency ratio range ($f_r < 0.2$) and returns the main signal as the first IMF at the end of the frequency ratio range ($f_r > 0.8$). In fact, as the LF component gets closer to the HF component by increasing the frequency ratio, both IMFs start to deviate from their corresponding components, and simultaneously, the first IMF commences to approach the main signal. There is always a frequency ratio in which the EMD behavior is changed and tends to give back the main signal instead of the signal's components. This frequency ratio is referred to as the cut-off frequency ratio and can be seen as a color change from white (lower error region) to black (higher error region). Generally, the larger cut-off frequency ratio indicates a higher tone separation ability. For $a_r < 1$, the cut-off frequency ratio is almost independent of the amplitude ratio and is near 0.67, but for $a_r > 1$, it decreases with the amplitude ratio increasing. Although

in this region, the cut-off frequency ratio has severe fluctuations, Rilling and Flandrin (2007) proposed two border curves that bound the cut-off frequency ratio. These curves are $a_r f_r = 1$ and $a_r f_r^2 = 1$, which are plotted by the continuous and dashed red lines, respectively. We also add another curve $a_r f_r^3 = 1$, which is represented by the dotted red line.

The middle diagram illustrates the superiority of the SIP$_1$-EMD over the traditional EMD. While the cut-off frequency ratio (the border between black and white regions) of the traditional EMD lies between curves of $a_r f_r = 1$ and $a_r f_r^2 = 1$, it completely crosses the $a_r f_r^2 = 1$ curve, applying the SIP$_1$-EMD, so in the middle diagram, the cut-off frequency ratio is located between curves of $a_r f_r^2 = 1$ and $a_r f_r^3 = 1$. Similarly, the SIP$_2$-EMD leads the cut-off frequency ratio beyond the curve $a_r f_r^3 = 1$ in the bottom diagram. Considering that the horizontal axes of these diagrams are logarithmic, SIP$_1$-EMD and SIP$_2$-EMD methods significantly increase the percentage of the white-colored area. If we define the frequency resolution as the power of distinguishing between two adjacent spectral components, the growth of the white-colored area by the SIP$_1$-EMD and SIP$_2$-EMD methods can be interpreted as the improvement of the frequency resolution. It should be noted again that Fig. 4 consists of 100 000 different signals, so the improvements in the results are not random.

To conduct an in-depth analysis of the impact of SIP on EMD, we assign three different constant values to the frequency ratio ($f_r = 0.6$, 0.65, and 0.7) and investigate the TSE as a function of the amplitude ratio. Abrupt change of the TSE value occurs in a specific amplitude ratio. We define the n-th critical amplitude ratio as:

$$a_{r,c_n} = \frac{1}{f_r^n}, \qquad n = 1, 2, 3, \ldots . \tag{8}$$

Figure 5 shows that the SIP$_1$-EMD and SIP$_2$-EMD extend the acceptable error range at least to $[01/f_r^2]$ and $[01/f_r^3]$, respectively.

A question that should be answered here is whether increasing the number of sifting iterations in the traditional EMD can always reduce the TSE. In other words, could increasing the number of sifting iterations substitute for SIP$_1$-EMD and SIP$_2$-EMD methods? To answer this question, three two-component signals with the same frequency ratio ($f_r = 0.65$) and different amplitude ratios (a_r = 2, 3, and 4) are selected and their TSE are computed for different sifting iterations.

Figure 6 represents the TSE in terms of the number of sifting iterations. In the first case ($a_r = 2$), the traditional EMD does not return an acceptable response even after 10000 iterations, while both SIP$_1$-EMD and SIP$_2$-EMD converge to low error just after 60 iterations. The coincidence of the SIP$_1$-EMD and SIP$_2$-EMD curves in the top diagram comes from

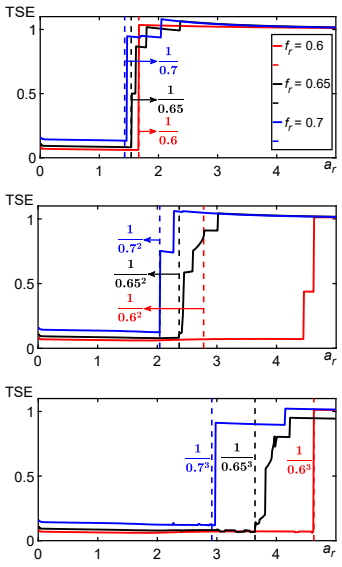

Fig. 5. TSE values as a function of a_r for $f_r = 0.6$ (red), 0.65 (black), and 0.7 (blue), with 100 fixed number of sifting iterations. The critical amplitude ratios are plotted by vertical dashed lines in each diagram. Top – TSE of the traditional EMD, the critical amplitude ratio is $a_{r,c_1} = 1/f_r$; middle – TSE of the SIP$_1$-EMD, the critical amplitude ratio is $a_{r,c_2} = 1/f_r^2$; bottom – TSE of the SIP$_2$-EMD, the critical amplitude ratio is $a_{r,c_3} = 1/f_r^3$.

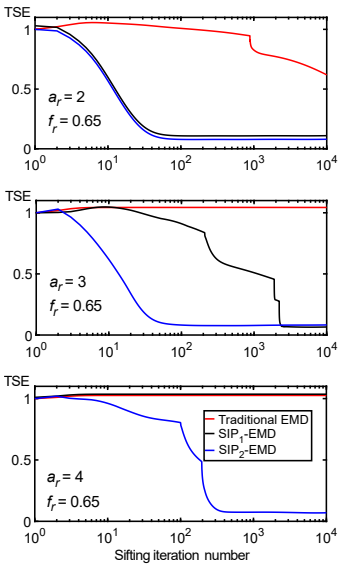

Fig. 6. TSE of three two-tone signals as a function of the number of sifting iterations. Signals have the same frequency ratio ($f_r = 0.65$) but different amplitude ratios (top diagram – $a_r = 2$; middle diagram – $a_r = 3$; bottom diagram $a_r = 4$). TSE values are calculated using the traditional EMD (red), SIP$_1$-EMD (black), and SIP$_2$-EMD (blue).

the fact that in the first case, the signal has some SIP$_1$, but it does not have any SIP$_2$, so the SIP$_2$-EMD gains no more benefits here. In the middle diagram ($a_r = 3$), the traditional EMD cannot decompose the signal at all. The SIP$_1$-EMD and SIP$_2$-EMD methods

converge to low error levels after 2500 and 70 sifting iterations, respectively. The benefit of the SIP_2-EMD, in this case, is its lower computational cost. In the third case ($a_r = 4$), which is plotted in the bottom diagram, neither the traditional EMD nor the SIP_1-EMD can decompose the signal, but SIP_2-EMD separates the signal's components after 400 iterations. The advantage of the SIP_2-EMD is more apparent here.

5.2. Vibration signal of a rolling bearing

Rolling element bearings are one of the most important components of rotating machines, and their failure may cause machinery breakdowns or safety hazards. Among the existing bearing fault diagnosis methods, vibration signal processing stands out for its accuracy, applicability, and simplicity.

Using EMD (traditional or modified variants) as the main decomposition method or along with other methods for bearing fault diagnosis has been the subject of many studies in recent years (Lei *et al.*, 2013; Guo, Deng, 2017). Sun *et al.* (2021) presented a novel bearing fault diagnosis on the basis of the EMD and improved Chebyshev distance. Shu *et al.* (2022) used modified CEEMDAN and the modified hierarchical amplitude-aware permutation entropy (MHAAPE) to decide whether the bearing was healthy and accurately identify different fault states in the bearings. Wang *et al.* (2022) studied a fault feature extraction method of variable speed rolling bearings based on statistical complexity measures (SCM). The SCM selects the optimal IMF component and evaluates an index for the optimal response of stochastic resonance. Zheng *et al.* (2022) proposed a spectral envelope-based adaptive empirical Fourier decomposition (SEAEFD) method and compared its performance with some other methods, including EMD.

The occurrence of any fault in any part of the bearing, including the inner race, outer race, rolling elements, and the cage, can be diagnosed by its specific frequency.

In the top row of Fig. 7, a typical acceleration signal $y_{FB}(t)$ of a faulty bearing is shown as a function of time. This signal is taken from the bearing data center of Case Western Reserve University (Case Western Reserve University [CWRU], n.d.). The CWRU Bearing Data Center has provided access to valuable datasets of normal and faulty bearing acceleration signals. These datasets are frequently used as reference signals in the majority of bearing diagnostic studies. The ball pass frequency of the inner race (BPFI) of this bearing is approximately 162 Hz (SKF, n.d.). Further information about the categories of datasets, test stand, bearing details and experimental conditions are presented in (CWRU, n.d.; Smith, Randall, 2015).

To assess the ability of the proposed EMD method to separate different modes, a simple sinusoidal function $y_2(t)$ with variable amplitude and frequency is added to the faulty bearing signal as follows:

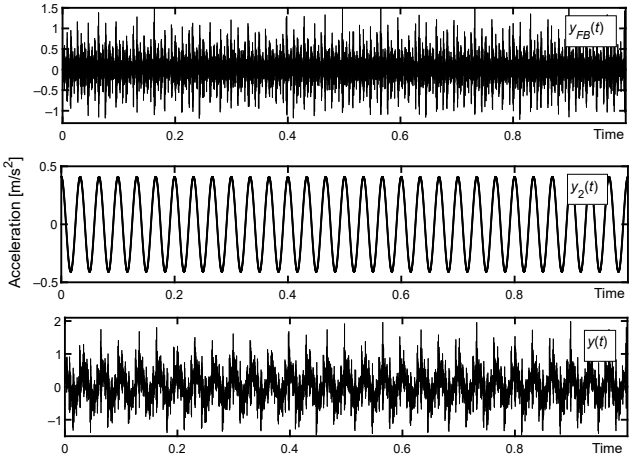

Fig. 7. Acceleration signal of the faulty bearing, $y_{FB}(t)$ (top), simple cosine function with $a_r = 1$ and $f_2 = 30$ Hz, $y_2(t)$ (middle), and a combination of them, $y(t)$ (bottom).

$$y(t) = y_1(t) + y_2(t) = y_{FB}(t) + a_r\left(\sqrt{2}\mathrm{RMS}\left(y_{FB}(t)\right)\right)\cos(2\pi f_2 t), \quad (9)$$

where f_2 is the frequency of $y_2(t)$, and a_r is the ratio of the root mean square (RMS) of $y_2(t)$ to the RMS of $y_1(t)$, e.g., $a_r = 1$ means that the energy of the two terms is the same. Thus, the vibration signal $y(t)$ may be considered the superposition of two distinct defects, $y_1(t)$, which is the signal of the faulty bearing with inner race fault, and $y_2(t)$, which can be, for example, a signal of an unbalanced rotor ($f_2 = 30$ Hz). The parameter a_r explains the severity of two defects relative to each other. These three time signals $y_1(t)$, $y_2(t)$, and $y(t)$ are plotted in the top, middle, and bottom rows of Fig. 7, respectively. The duration of the original $y_{FB}(t)$ is more than 10 s, but only the first second of it is used to reduce the computational time in all calculations of this paper.

Unlike the deterministic synthetic signals of the previous sections, the components of the bearing nondeterministic signal are unknown. Hence, we will define some criteria for evaluating the performance of the traditional and SIP-EMD.

Figure 8 shows the first nine IMFs of the vibration signal $y(t)$ (with $a_r = 1$ and $f_2 = 30$ Hz) and their residual after extraction of the ninth IMFs. The results of the traditional EMD and the SIP_1-EMD are displayed in the left and right columns, respectively. In this figure, only the first tenth of the second of IMFs are drawn for better clarity of the graphs. But all calculations are performed within one second, as mentioned before. Due to the noise and sampling frequency restrictions in real-world signals, the traditional EMD is only compared with the SIP_1-EMD in this section.

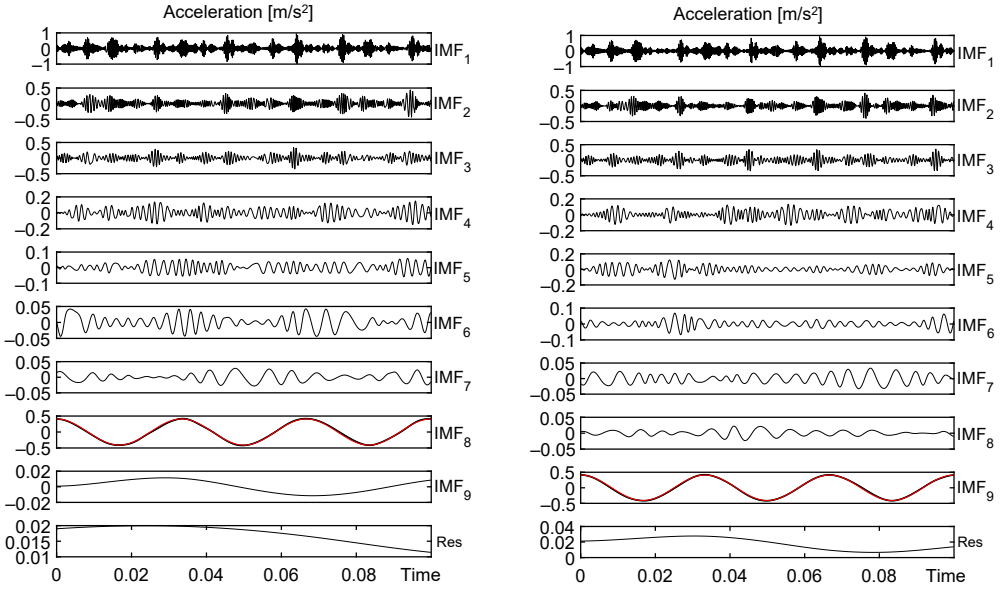

Fig. 8. First nine IMFs and residual of the vibration signal $y(t)$ (with $a_r = 1$ and $f_2 = 30$ Hz) for the traditional EMD (left) and the SIP$_1$-EMD (right). All IMFs and residuals are plotted with black lines, while $y_2(t)$ is plotted with the red line.

After the extraction of all IMFs, one of them shows the highest similarity with the cosine function $y_2(t)$. From now on, this IMF is called IMF*, which is plotted with black lines and fits well with the ideal cosine function $y_2(t)$ plotted with red lines in the eighth and ninth rows of the left and right columns of Fig. 8, respectively.

The SIP$_1$-EMD method extracts one more IMF than the traditional EMD. Although it should not be listed as an advantage by itself for either method, it must be taken into account in interpreting the results. The RMS of the difference between the IMF* with the ideal cosine function $y_2(t)$ will be applied as the first evaluation criterion (EC) as follows:

$$\mathrm{EC}_1 = \mathrm{RMSE} = \mathrm{RMS}(\mathrm{IMF}^* - y_2). \tag{10}$$

The errors of the traditional and SIP$_1$-EMD in this example are 0.013 and 0.009, respectively, which shows the better coincidence of the IMF* and y_2 in the SIP$_1$-EMD method.

To have an idea of energy conservation after decomposition, the index of energy conservation (IEC) is defined as the sum of the energies of all IMFs divided by the energy of the signal without considering the residual (Chen *et al.*, 2006). In this paper, the parameter IEC is considered as the second EC:

$$\mathrm{EC}_2 = \mathrm{IEC} = \frac{\sum_{i=1}^{N}\sum_{t}|\mathrm{IMF_i}(t)|^2}{\sum_{t}|y(t) - \mathrm{Res}(t)|^2}, \tag{11}$$

where N is the number of extracted IMFs. Values greater or less than one indicate the generation or leakage of energy during the sifting process. In this example, the IECs for the extracted IMFs of the traditional and SIP$_1$-EMD are 1.022 and 1.005, respectively, which shows better energy conservation in the SIP$_1$-EMD method.

The existence of spectral peaks at the bearing fault frequencies, their harmonics, and sidebands should be examined to detect the bearing faults. For example, a faulty bearing with a fault on its inner race should have a clear spectral peak at the BPFI, its harmonics, and sidebands. The spectrums of the most important IMFs of the traditional and SIP$_1$-EMD are displayed in the left and right columns of Fig. 9, respectively. The spectrums of other IMFs are omitted for the sake of brevity. In this special case with $f_2 = 30$ Hz, however, it can be shown empirically that the BPFI (162 Hz) content emerges in one or two IMFs before the IMF* (30 Hz). Here, the amplitudes of frequency spectrums are investigated at the BPFI (162 Hz), its harmonics (162 k, $k = 1, 2, 3, ...$), and sidebands of the BPFI and its harmonics (162 $k \pm 30$, $k = 1, 2, 3, ...$). The locations of the BPFI harmonics, their sidebands, and the shaft rotation frequency are indicated by the vertical continuous red lines, dashed red lines, and blue lines in Fig. 9, respectively. All amplitudes of this figure are normalized to the RMS of amplitudes for each frequency spectrum. This normalized amplitude is defined as the third EC as follows:

$$\mathrm{EC}_3 = \mathrm{Max}\left\{\frac{\mathrm{IMF}_i(\mathrm{BPFI})}{\mathrm{RMS}(\mathrm{IMF}_i)}\right\}, \qquad i = 1, 2, ..., N, \tag{12}$$

where IMF_i is the frequency spectrum of the i-th IMF. The first three rows of Fig. 9 show that the SIP$_1$-EMD produces higher spectral peaks at the BPFI than the traditional EMD method.

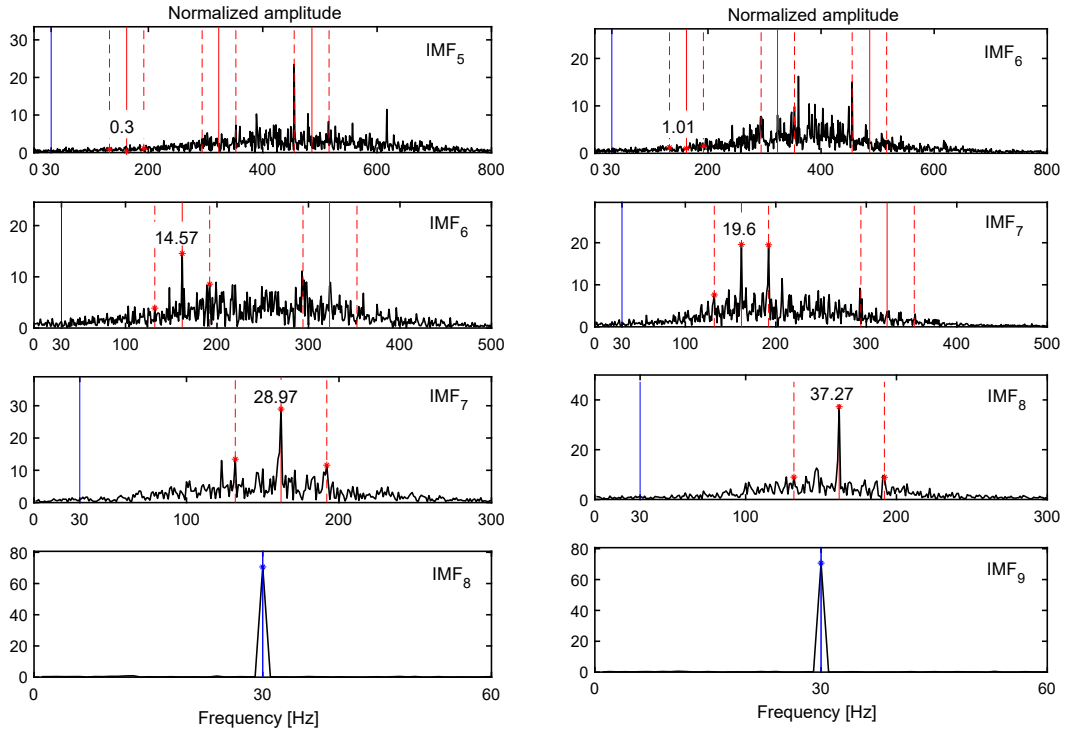

Fig. 9. Spectrums of the most important IMFs of the vibration signal $y(t)$ (with $a_r = 1$ and $f_2 = 30$ Hz) for the traditional EMD (left) and SIP$_1$-EMD (right). The shaft rotation frequency (30 Hz) is indicated with the vertical blue lines, the BPFI (162 Hz) and its harmonics are indicated with the vertical continuous red lines, and the sidebands (±30 Hz) of the BPFI and its harmonics are plotted with the vertical dashed red lines.

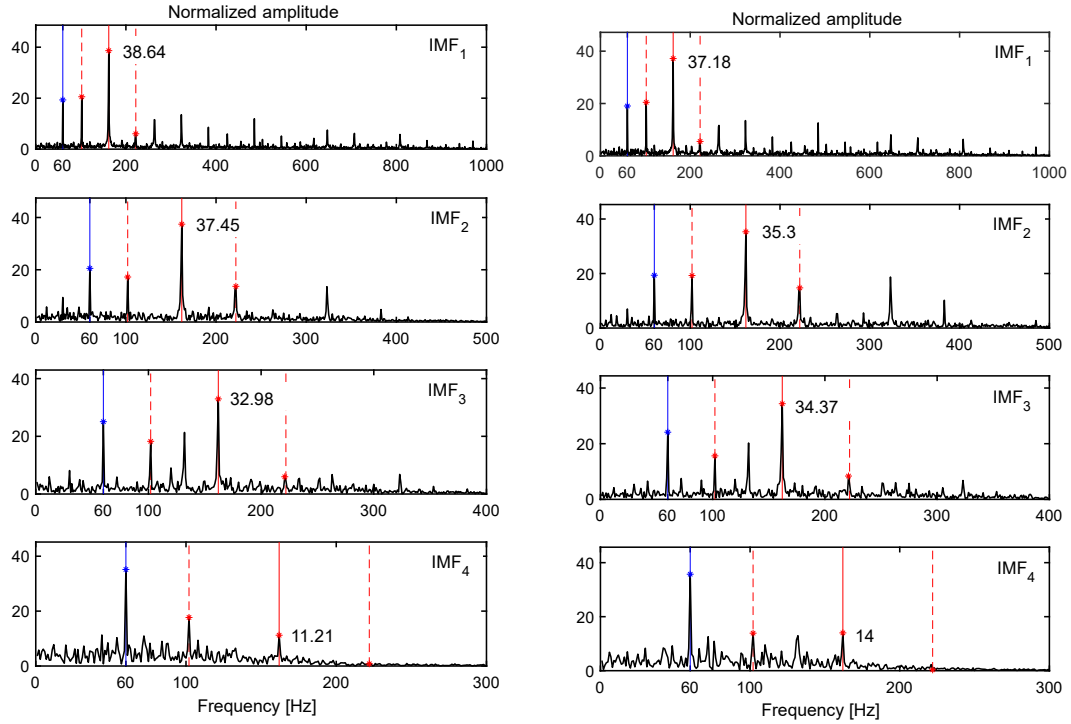

Fig. 10. Spectrums of envelopes for the first four IMFs of the vibration signal $y(t)$ (with $a_r = 1$ and $f_2 = 30$ Hz) extracted by the traditional EMD (left) and SIP$_1$-EMD (right). The shaft twice rotation frequency (60 Hz) is indicated with the vertical blue lines, the BPFI (162 Hz) is indicated with the vertical continuous red lines, and the sidebands of the BPFI (162 ± 60 Hz) are plotted with the vertical dashed red lines.

The envelope of the raw signal contains more diagnostic information than the raw signal itself. Hence, the spectrum of the envelope curves for the four IMFs of the traditional and the SIP$_1$-EMD are plotted in the left and right columns of Fig. 10, respectively. The spectral peaks are clearly evident at the BPFI (162 Hz) and its sidebands (132 and 192 Hz), especially in the first four IMFs. Then they continue to become shorter until they vanish at the final envelope spectrums. The fourth EC is defined as follows:

$$\mathrm{EC}_4 = \mathrm{Max}\left\{\frac{\mathrm{env}_i(\mathrm{BPFI})}{\mathrm{RMS}(\mathrm{env_i})}\right\}, \qquad i = 1, 2, ..., N, \quad (13)$$

where env_i is the spectrum of the envelope of the IMF_i. As shown in Fig. 10, the traditional EMD method produces higher spectral peaks at the first and second IMF envelopes, while the SIP$_1$-EMD method produces higher spectral peaks at the third and fourth IMF envelopes. This is partly due to the abovementioned additional IMF of the SIP$_1$-EMD method; consequently, the vibratory energy of the faulty bearing is distributed into one more IMF. Hence, the final EC is defined according to the average of spectral peaks:

$$\mathrm{EC}_5 = \mathrm{Mean}\left\{\frac{\mathrm{env}_i(\mathrm{BPFI})}{\mathrm{RMS}(\mathrm{env_i})}\right\}, \qquad i = 1, 2, ..., 4. \quad (14)$$

The evaluation criteria of the traditional EMD and SIP$_1$-EMD methods for the decomposition of the faulty bearing vibration signal with and without the added sinusoidal function are presented in Table 1. In the absence of the added cosine function ($a_r = 0$), the first evaluation criterion does not make sense. The better performance in each case is emphasized with a bold font in the table. The results show the superiority of the SIP$_1$-EMD method to the traditional EMD method in all items except for EC$_4$, the reason for which was mentioned before.

To investigate the performance of the proposed SIP$_1$-EMD method in a wider frequency range, the frequency of the sinusoidal term (f_2) is assumed to be a variable parameter that varies from 10 Hz to 100 Hz. In this case, the amplitude ratio is considered a constant value of one ($a_r = 1$). The values of all evaluation criteria are then calculated and plotted with blue and red lines for the traditional EMD and SIP$_1$-EMD methods, respectively, in Fig. 11. The horizontal axis of all graphs in this figure is the frequency of the sinusoidal term in Hz. The results confirm the superiority of the SIP$_1$-EMD method to the traditional EMD through the specified frequency range for all evaluation criteria except for EC$_4$.

Table 1. Evaluation criteria of the traditional EMD and SIP$_1$-EMD for the decomposition of the vibration signal of the faulty bearing with (right column) and without (middle column) the added cosine term.

Evaluation criteria	$a_r = 0$		$a_r = 1$, $f_2 = 30$ Hz	
	Traditional EMD	SIP-EMD	Traditional EMD	SIP-EMD
EC$_1$: RMS of error	–	–	0.013	**0.009**
EC$_2$: Index of energy conservation	1.052	**1.011**	1.022	**1.005**
EC$_3$: Maximum spectral peak of IMFs	27.82	**28.27**	28.97	**37.27**
EC$_4$: Maximum spectral peak of IMF envelopes	**38.68**	37.23	**38.64**	37.18
EC$_5$: Average of spectral peaks of IMF envelopes	29.07	**30.26**	30.07	**30.21**

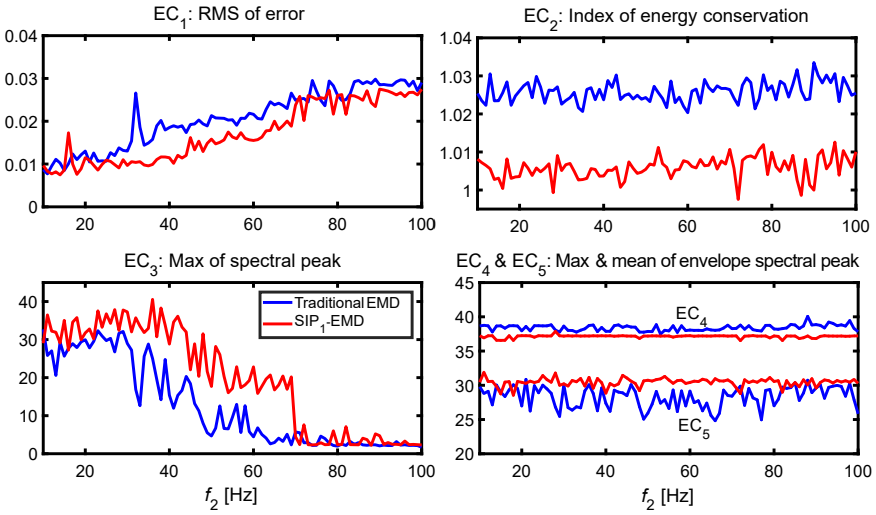

Fig. 11. Evaluation criteria for different signals with a variable frequency of f_2 = [10 to 100] Hz and a constant amplitude ratio of $a_r = 1$. The curves of the traditional-EMD and SIP$_1$-EMD methods are plotted with blue and red lines, respectively.

6. Conclusions

This paper evaluated how the interpolation points of the envelope curve affect the EMD results. In the traditional EMD, the extremum points of the signal are used as the interpolation points for the construction of the envelope curves. We propose to add new sets of interpolation points to the existing one. These new points are special inflection points of the signal (SIP_1), special inflection points of the first derivative of the signal (SIP_2), and so on to the special inflection points of the $(n-1)$ derivative of the signal (SIP_n). The results indicate that adding each of these sets to the previous interpolation points makes an obvious improvement in the tone separation ability of the EMD method. This claim was validated by the 2D diagram of the tone separation error on the $(a_r - f_r)$ plane, where the tone separation errors of more than 100 000 two-tone signals are plotted with different frequencies and amplitude ratios. If a signal itself does not have any SIP_n and no SIP_n appears in h_{ik} during the sifting process, the results of the traditional EMD will coincide with the SIP_n-EMD method. However, as soon as at least one SIP_n appears in the signal or during the sifting process, the SIP_n-EMD obtains a significant reduction in the error diagram, while the traditional EMD method either does not reduce the error at all or reduces the error after many times of sifting iterations. A vibration signal of a rolling element bearing with the inner race fault was analyzed to evaluate the effectiveness of both the traditional and SIP_n-EMD methods in the decomposition of a real-world signal. The results show a better performance of the proposed method in the fault feature extraction of the bearing.

Acknowledgments

This work was supported by the Mobarakeh Steel Company.

References

1. Bouchikhi A., Boudraa A.-O. (2012), Multicomponent AM–FM signals analysis based on EMD-B-splines ESA, *Signal Processing*, **92**(9): 2214–2228, doi: 10.1016/j.sigpro.2012.02.014.
2. Case Western Reserve University (n.d.), *Bearing Data Center*, https://engineering.case.edu/bearingdatacenter/download-data-file (access date: 21.02.2023).
3. Chen Q., Huang N., Riemenschneider S., Xu Y. (2006), A B-spline approach for empirical mode decompositions, *Advances in Computational Mathematics*, **24**(1): 171–195, doi: 10.1007/s10444-004-7614-3.
4. Chu P.C., Fan C., Huang N. (2012), Compact empirical mode decomposition: An algorithm to reduce mode mixing, end effect, and detrend uncertainty, *Advances in Adaptive Data Analysis*, **4**(3): 1250017, doi: 10.1142/S1793536912500173.
5. Deering R., Kaiser J.F. (2005), The use of a masking signal to improve empirical mode decomposition, [in:] *Proceedings (ICASSP'05). IEEE International Conference on Acoustics, Speech, and Signal Processing*, **4**: 485–488, doi: 10.1109/ICASSP.2005.1416051.
6. Egambaram A., Badruddin N., Asirvadam V.S., Begum T. (2016), Comparison of envelope interpolation techniques in empirical mode decomposition (EMD) for eyeblink artifact removal from EEG, [in:] *2016 IEEE EMBS Conference on Biomedical Engineering and Sciences (IECBES)*, pp. 590–595, doi: 10.1109/IECBES.2016.7843518.
7. Guo T., Deng Z. (2017), An improved EMD method based on the multi-objective optimization and its application to fault feature extraction of rolling bearing, *Applied Acoustics*, **127**: 46–62, doi: 10.1016/j.apacoust.2017.05.018.
8. Huang N.E *et al.* (1998), The empirical mode decomposition and the Hilbert spectrum for nonlinear and non-stationary time series analysis, *Proceedings of the Royal Society of London. Series A: Mathematical, Physical and Engineering Sciences*, **454**(1971): 903–995, doi: 10.1098/rspa.1998.0193.
9. Huang N.E. *et al.* (2003), A confidence limit for the empirical mode decomposition and Hilbert spectral analysis, *Proceedings of the Royal Society of London. Series A: Mathematical, Physical and Engineering Sciences*, **459**(2037): 2317–2345, doi: 10.1098/rspa.2003.1123.
10. Kopsinis Y., McLaughlin S. (2007), Investigation and performance enhancement of the empirical mode decomposition method based on a heuristic search optimization approach, [in:] *IEEE Transactions on Signal Processing*, **56**(1): 1–13, doi: 10.1109/TSP.2007.901155.
11. Kopsinis Y., McLaughlin S. (2008), Improved EMD using doubly-iterative sifting and high order spline interpolation, *EURASIP Journal on Advances in Signal Processing*, **2008**(1): 128293, doi: 10.1155/2008/128293.
12. Lei Y., Lin J., He Z., Zuo M.J. (2013), A review on empirical mode decomposition in fault diagnosis of rotating machinery, *Mechanical Systems and Signal Processing*, **35**(1–2): 108–126, doi: 10.1016/j.ymssp.2012.09.015.
13. Li H., Qin X., Zhao D., Chen J., Wang P. (2018), An improved empirical mode decomposition method based on the cubic trigonometric B-spline interpolation algorithm, *Applied Mathematics and Computation*, **332**: 406–419, doi: 10.1016/j.amc.2018.02.039.
14. Li H., Wang C., Zhao D. (2015a), An improved EMD and its applications to find the basis functions of EMI signals, *Mathematical Problems in Engineering*, **2015**: 150127, doi: 10.1155/2015/150127.
15. Li Y., Xu M., Wei Y., Huang W. (2015b), An improvement EMD method based on the optimized rational Hermite interpolation approach and its application to gear fault diagnosis, *Measurement*, **63**: 330–345, doi: 10.1016/j.measurement.2014.12.021.

16. Pegram G.G.S., Peel M.C., McMahon T.A. (2008), Empirical mode decomposition using rational splines: An application to rainfall time series, *Proceedings of the Royal Society A: Mathematical, Physical and Engineering Sciences*, **464**(2094): 1483–1501, doi: 10.1098/rspa.2007.0311.

17. Qin S.R., Zhong Y.M. (2006), A new envelope algorithm of Hilbert–Huang Transform, *Mechanical Systems and Signal Processing*, **20**(8): 1941–1952, doi: 10.1016/j.ymssp.2005.07.002.

18. Rilling G., Flandrin P. (2007), One or two frequencies? The empirical mode decomposition answers, [in:] *IEEE Transactions on Signal Processing*, **56**(1): 85–95, doi: 10.1109/TSP.2007.906771.

19. Rilling G., Flandrin P., Gonçalvès P. (2003), On empirical mode decomposition and its algorithms, [in:] *IEEE-EURASIP workshop on nonlinear signal and image processing*, **3**(3): 8–11, Grado.

20. Shu L., Deng H., Liu X., Pan Z. (2022), A Comprehensive working condition identification scheme for rolling bearings based on modified CEEMDAN as well as modified hierarchical amplitude-aware permutation entropy, *Measurement Science and Technology*, **33**(7): 075111, doi: 10.1088/1361-6501/ac5b2c.

21. Singh P., Joshi S.D., Patney R.K., Saha K. (2014), Some studies on nonpolynomial interpolation and error analysis, *Applied Mathematics and Computation*, **244**: 809–821, doi: 10.1016/j.amc.2014.07.049.

22. SKF (n.d.), *Bearing Select*, https://www.skfbearingselect.com/#/bearing-selection-start (access date: 21.02.2023).

23. Smith W.A., Randall R.B. (2015), Rolling element bearing diagnostics using the Case Western Reserve University data: A benchmark study, *Mechanical Systems and Signal Processing*, **64–65**: 100–131, doi: 10.1016/j.ymssp.2015.04.021.

24. Sun Y., Li S., Wang X. (2021), Bearing fault diagnosis based on EMD and improved Chebyshev distance in SDP image, *Measurement*, **176**: 109100, doi: 10.1016/j.measurement.2021.109100.

25. Torres M.E., Colominas M.A., Schlotthauer G., Flandrin P. (2011), A complete ensemble empirical mode decomposition with adaptive noise, [in:] *2011 IEEE International Conference on Acoustics, Speech and Signal Processing (ICASSP)*, pp. 4144–4147, doi: 10.1109/ICASSP.2011.5947265.

26. Wang J., Du G., Zhu Z., Shen C., He Q. (2020), Fault diagnosis of rotating machines based on the EMD manifold, *Mechanical Systems and Signal Processing*, **135**: 106443, doi: 10.1016/j.ymssp.2019.106443.

27. Wang J.-L., Li Z.-J. (2013), Extreme-point symmetric mode decomposition method for data analysis, *Advances in Adaptive Data Analysis*, **5**(3): 1350015, doi: 10.1142/S1793536913500155.

28. Wang Z., Yang J., Guo Y. (2022), Unknown fault feature extraction of rolling bearings under variable speed conditions based on statistical complexity measures, *Mechanical Systems and Signal Processing*, **172**: 108964, doi: 10.1016/j.ymssp.2022.108964.

29. Wu Z., Huang N.E. (2009), Ensemble empirical mode decomposition: A noise-assisted data analysis method, *Advances in Adaptive Data Analysis*, **1**(1): 1–41, doi: 10.1142/S1793536909000047.

30. Xu Z., Huang B., Li K. (2010), An alternative envelope approach for empirical mode decomposition, *Digital Signal Processing*, **20**(1): 77–84, doi: 10.1016/j.dsp.2009.06.009.

31. Yang L., Yang Z., Zhou F., Yang L. (2014), A novel envelope model based on convex constrained optimization, *Digital Signal Processing*, **29**(1): 138–146, doi: 10.1016/j.dsp.2014.02.017.

32. Yeh J.-R., Shieh J.-S., Huang N.E. (2010), Complementary ensemble empirical mode decomposition: A novel noise enhanced data analysis method, *Advances in Adaptive Data Analysis*, **2**(2): 135–156, doi: 10.1142/S1793536910000422.

33. Yuan J., He Z., Ni J., Brzezinski A.J., Zi Y. (2013), Ensemble noise-reconstructed empirical mode decomposition for mechanical fault detection, *Journal of Vibration and Acoustics*, **135**(2): 021011, doi: 10.1115/1.4023138.

34. Yuan J., Xu C., Zhao Q., Jiang H., Weng Y. (2022), High-fidelity noise-reconstructed empirical mode decomposition for mechanical multiple and weak fault extractions, *ISA Transaction*, **129**(Part B): 380–397, doi: 10.1016/j.isatra.2022.02.017.

35. Zhao D., Huang Z., Li H., Chen J., Wang P. (2017), An improved EEMD method based on the adjustable cubic trigonometric cardinal spline interpolation, *Digital Signal Processing*, **64**: 41–48, doi: 10.1016/j.dsp.2016.12.007.

36. Zheng J., Cao S., Pan H., Ni Q. (2022), Spectral envelope-based adaptive empirical Fourier decomposition method and its application to rolling bearing fault diagnosis, *ISA Transactions*, **129**(Part B): 476–492, doi: 10.1016/j.isatra.2022.02.049.